

Redshift Evolution of the Fundamental Plane Relation in the IllustrisTNG Simulation

Shengdong Lu^{1,2★}, Dandan Xu³, Yunchong Wang^{4,3}, Shude Mao^{3,1}, Junqiang Ge¹,
Volker Springel⁵, Yuan Wang⁶, Mark Vogelsberger⁷, Jill Naiman^{8,9}, Lars Hernquist⁸

¹National Astronomical Observatories, Chinese Academy of Sciences, 20A Datun Road, Chaoyang District, Beijing 100101, China

²University of Chinese Academy of Sciences, Beijing 100049, China

³Department of Astronomy and Tsinghua Center for Astrophysics, Tsinghua University, Beijing 100084, China

⁴Department of Physics, Tsinghua University, Beijing, 100084, China

⁵Max-Planck-Institut für Astrophysik, Karl-Schwarzschild-Str. 1, D-85748, Garching, Germany

⁶School of Physics, Nankai University, Tianjin 300071, China

⁷Kavli Institute for Astrophysics and Space Research, Department of Physics, MIT, Cambridge, MA 02139, USA

⁸Harvard-Smithsonian Center for Astrophysics, 60 Garden Street, Cambridge, MA, 02138, USA

⁹The School of Information Sciences at the University of Illinois Urbana-Champaign, 501 E Daniel St, Champaign, IL 61820, USA

Accepted ***, Received ***, in original form ***

ABSTRACT

We investigate the fundamental plane (FP) evolution of early-type galaxies in the IllustrisTNG-100 simulation (TNG100) from redshift $z = 0$ to $z = 2$. We find that a tight plane relation already exists as early as $z = 2$. Its scatter stays as low as ~ 0.08 dex across this redshift range. Both slope parameters b and c (where $R \propto \sigma^b I^c$ with R , σ , and I being the typical size, velocity dispersion, and surface brightness) of the plane evolve mildly since $z = 2$, roughly consistent with observations. The FP residual $\text{Res} (\equiv a + b \log \sigma + c \log I - \log R$, where a is the zero point of the FP) is found to strongly correlate with stellar age, indicating that stellar age can be used as a crucial fourth parameter of the FP. However, we find that $4c + b + 2 = \delta$, where $\delta \sim 0.8$ for FPs in TNG, rather than zero as is typically inferred from observations. This implies that a tight power-law relation between the dynamical mass-to-light ratio M_{dyn}/L and the dynamical mass M_{dyn} (where $M_{\text{dyn}} \equiv 5\sigma^2 R/G$, with G being the gravitational constant) is not present in the TNG100 simulation. Recovering such a relation requires proper mixing between dark matter and baryons, as well as star formation occurring with correct efficiencies at the right mass scales. This represents a powerful constraint on the numerical models, which has to be satisfied in future hydrodynamical simulations.

Key words: galaxies: elliptical and lenticular, cD – galaxies: formation – galaxy: evolution – galaxy: kinematics and dynamics – methods: numerical

1 INTRODUCTION

Early-type galaxies (ETGs) are the final products of the hierarchical assembly of galaxies via mergers and accretion (e.g., Toomre & Toomre 1972; Bender et al. 1992). They are found to obey several empirical scaling relations, e.g., the Faber-Jackson relation (Faber & Jackson 1976) between a galaxy’s velocity dispersion σ and its luminosity L , the relation between the supermassive black hole mass M_{BH} and its host galaxy bulge’s luminosity L or velocity dispersion σ (Kormendy & Richstone 1995; Magorrian et al. 1998; Ferrarese & Merritt 2000; Husemann et al. 2016; Subramanian et al. 2016), as well as the famous Fundamental Plane (FP) relation (Djorgovski & Davis 1987; Dressler et al. 1987; Jørgensen

et al. 1996; Cappellari et al. 2006; La Barbera et al. 2008) that exists between galaxy size R , velocity dispersion σ , and surface brightness $I \equiv L/(\pi R^2)$.

In particular, the tight FP relation reflects correlations among a galaxy’s structural properties, dynamics, and star-formation activities. The FP can be expressed as:

$$\log R = a + b \log \sigma + c \log I, \quad (1)$$

where a , b and c are the plane variables. The origin of the FP can be understood from virial theorem (Faber et al. 1987), which links a galaxy’s gravitational potential energy $-GM_{\text{tot}}^2/R$ with its kinetic energy $T_{\text{kin}} \propto M_{\text{tot}}\sigma^2/2$, where M_{tot} is the total mass of a galaxy; R and σ are characteristic size and velocity dispersion measurements. Rewriting M_{tot} in terms of luminosity L and a total mass-to-light ratio M_{tot}/L , the virial theorem can be translated into a plane rela-

★ E-mail: lushengdong@nao.cas.cn

tion:

$$\log R = K_{SD} + 2 \log \sigma - \log I - \log M_{tot}/L, \quad (2)$$

where K_{SD} is a normalization factor depending on a galaxy's structural properties and dynamics (see [Taranu et al. 2015](#) for a more detailed discussion on this topic). The observed FP relation typically has parameters $b \neq 2$ and $c \neq -1$, which may not necessarily mean the breakdown of the virial theorem. It also manifests a breakdown of homologies in galactic structural and dynamical distributions, i.e., constant K_{SD} (e.g., [Ciotti et al. 1996](#); [Pahre et al. 1998a,b](#); [Bertin et al. 2002](#); [Trujillo et al. 2004](#); [Saglia et al. 2010](#)) as well as of constant mass-to-light ratios M_{tot}/L (e.g., [Pahre et al. 1995](#); [Cappellari 2016](#), also see references below). Non-homologies and non-constant M_{tot}/L ratios can be caused by, for example, variations in the density profiles (e.g., [Schombert 1986](#)), in the velocity dispersion anisotropies (e.g., [Davies et al. 1983](#); [Busarello et al. 1992](#); [Ciotti et al. 1996](#); [Nipoti et al. 2002](#)), in the different spatial distributions of dark matter and visible matter (e.g., [Ciotti et al. 1996](#); [Humphrey & Buote 2010](#)), as well as in the stellar initial mass function (IMF), resulting in different stellar populations (e.g., [Renzini & Ciotti 1993](#)). Such non-homologies have been observed in galaxies of different masses, with different formation histories, and in different environments (e.g., [Pahre et al. 1998b](#); [van Dokkum et al. 2001](#); [Bernardi et al. 2003](#); [Lanzoni et al. 2003](#); [Bernardi et al. 2006](#); [Saglia et al. 2010](#)).

The tightness of the *observed* FP is even stronger when the relation is translated into the so-called κ -space ([Bender et al. 1992](#)) via an orthogonal transformation. By assuming a so-called 'dynamical mass' $M \propto \sigma^2 R$, this edge-on view can be interpreted as the FP projected onto the $\log M/L - \log M$ plane, with the dynamical mass taking the mathematical form:

$$\log M = A + 2 \log \sigma + \log R, \quad (3)$$

where A is a normalization factor (e.g., [Faber et al. 1987](#); [van Albada et al. 1995](#)). By invoking an exact power-law relation between M/L and M , i.e., $M/L \propto M^\alpha$, where $\alpha > 0$ reflects that more massive galaxies have larger mass-to-light ratios (also referred to as the so-called 'tilt of the FP¹'), we have another alternative relation after rewriting M and L in terms of R , σ , and I :

$$\log R = A' + \frac{2(1-\alpha)}{1+\alpha} \log \sigma + \frac{-1}{1+\alpha} \log I, \quad (4)$$

where A' is a normalization factor. Comparing this with Eq.(1), we find:

$$\begin{cases} \frac{2(1-\alpha)}{1+\alpha} = b, \\ \frac{-1}{1+\alpha} = c. \end{cases} \quad (5)$$

Thus, to derive the power-law relation between M/L and M , we must have:

$$\begin{cases} 4c + b + 2 = 0, \\ \alpha = 1 + \frac{b}{2c}. \end{cases} \quad (6)$$

Observed early-type galaxies broadly satisfy these relations at various redshifts extending to $z > 1$ (e.g., [Bender et al. 1992](#); [Jørgensen et al. 1996, 2006](#); [Hyde & Bernardi 2009](#); [Cappellari et al. 2013](#)).

¹ Note that homologies in K_{SD} and M/L , i.e., plane parameters of $b = 2$ and $c = -1$ correspond to $\alpha = 0$, i.e., M/L being independent of galaxy mass M .

Many studies have tried to understand why such a tight correlation between the dynamical mass and the dynamical mass-to-light ratio exists for early-type galaxies, but it is not yet fully understood (e.g., [Renzini & Ciotti 1993](#); [Ciotti et al. 1996](#); [Graham & Colless 1997](#); [Pahre et al. 1998a](#)).

One of the many utilities of the FP relation that is directly relevant to galaxy formation studies, is to use the offset of the plane's intercept a from its local ($z = 0$) zero point value to measure the redshift evolution of the mass-to-light ratio M/L , from which halo assembly histories (through the evolution of the galaxy mass) as well as star-formation histories (through the age of the stellar population) can be further inferred. This has been routinely carried out for observed early-type galaxies (e.g., [van Dokkum & Franx 1996](#); [Bender et al. 1998](#); [van de Ven et al. 2003](#); [Jørgensen et al. 2006](#)). For this to work out, a couple of assumptions need to be made in practice. It is easy to show that under Eq. (3), the corresponding dynamical mass-to-light ratio M/L can be expressed in terms of FP variables:

$$\log M/L = (2c+b)/c \log \sigma - (1+c)/c \log R + [a/c - \log \pi + A]. \quad (7)$$

The change of the mass-to-light ratio $\Delta \log M/L$ over cosmic times can then be written as:

$$\Delta \log M/L = \Delta[(2c+b)/c \log \sigma] + \Delta[-(1+c)/c \log R] + \Delta[a/c]. \quad (8)$$

As can be seen, the redshift evolution of M/L can result from galaxy structural and dynamical evolution (due to ΔR and $\Delta \sigma$), from the 'rotation' of the FP (due to Δb and Δc), and from changes in the plane's zero point (due to Δa) over cosmic time.

Suppose we are allowed to assume that the FP slope parameters b and c change little within a given redshift range, then Eq. (8) reduces to:

$$\Delta \log M/L = (2c+b)/c \Delta \log \sigma - (1+c)/c \Delta \log R + (\Delta a)/c. \quad (9)$$

Further assuming that (i) the dynamical mass of an early-type galaxy does not change significantly within a given redshift range, i.e., $\Delta \log M = 0$ thus $\Delta \log R = -2\Delta \log \sigma$, plus that Eq. (6) stands; or alternatively (ii) the velocity dispersion and size of the galaxy does not vary much within a given redshift range, i.e., $\Delta \log \sigma = 0$ and $\Delta \log R = 0$, then Eq. (9) reduces to:

$$\Delta \log M/L = (\Delta a)/c. \quad (10)$$

As can be seen, when all the involved assumptions approximately hold, it is possible to estimate the evolution of M/L by a simple approximation using the FP zero point offset in combination with the local FP parameters, as indicated by Eq. (10). Observed early-type galaxies seem to more or less obey some of the key assumptions listed above, but not necessarily all. For example, the FP slopes b and c are observed to have experienced some moderate evolution with cosmic time (e.g., [di Serego Alighieri et al. 2005](#); [Treu et al. 2005](#); [Jørgensen et al. 2006](#); [Saglia et al. 2010](#)). Both morphological (size and shape) and dynamical evolution of early-type galaxies have been theoretically proposed (e.g., [Biermann & Shapiro 1979](#); [Kobayashi 2005](#); [Khochfar & Silk 2006](#); [Fan et al. 2008](#); [Hopkins et al. 2009](#); [Genel et al. 2018](#)), which are supported by observational evidence (e.g., [van Dokkum et al. 2008](#); [Saglia et al. 2010](#); [van der Wel et al. 2011](#); [Chevance et al. 2012](#)) and may result from various internal feedback processes as well as galaxy mergers. One should keep in mind, however, that any strong violation of the assumptions above could result in the derived luminosity evolution (through Eq. 10) differing from the actual redshift evolution and thus introducing uncertainties to the estimation. Furthermore, in reality, observational samples can be even more complicated due to various selection effects (e.g., [van der Wel et al. 2005](#)).

and progenitor bias (e.g., [van Dokkum et al. 2001](#); [Valentinuzzi et al. 2010](#); [Saglia et al. 2010](#)).

Accurate estimates of a FP’s zero point are closely related to another interesting feature (or the fourth parameter) of the plane, i.e., the plane’s scatter. Observed FPs, although tight, are found to possess some intrinsic scatter that cannot be explained purely by observational errors (see references listed above). The cause of this scatter has been attributed to variations in the stellar populations ([Gregg 1992](#); [Prugniel & Simien 1996](#); [Jørgensen et al. 2006](#)), in particular, their (post-merger) ages since the last major episode of star-formation (which are possibly triggered by gas-rich merger events) in these early-type galaxies ([Forbes et al. 1998](#); [Terlevich & Forbes 2002](#)). This in fact is also consistent with the theoretical expectation for early-type galaxies with a given dynamical mass at a fixed redshift: changes in luminosity among galaxies, as reflected by the variation of the plane’s zero point (see Eq. 10), result from the aging (passive evolution) of the stellar populations since their last major star-forming phase.

With the advancement of state-of-the-art numerical tools and collective efforts to simulate cosmic structure formation, a number of new-generation hydrodynamic cosmological simulations have been performed, which have significantly increased our abilities to understand galaxy formation within the current cosmology framework dominated by dark matter and dark energy. Projects of this type include the Illustris Simulations ([Genel et al. 2014](#); [Vogelsberger et al. 2014a,b](#); [Nelson et al. 2015](#)), the EAGLE Simulations ([Crain et al. 2015](#); [Schaye et al. 2015](#)), the Horizon-AGN project ([Dubois et al. 2014](#)), as well as the latest IllustrisTNG simulation² ([Marinacci et al. 2018](#); [Naiman et al. 2018](#); [Nelson et al. 2018](#); [Pillepich et al. 2018b](#); [Springel et al. 2018](#)) etc. These advanced cosmological simulations have provided us with large populations of galaxy samples, which agree with available observations to different degrees. Through detailed comparison analyses, one can not only calibrate the modelling parameters and guide the interpretation of observations, but also identify improper model treatment of the sub-grid physics in these simulations. [Rosito et al. \(2019\)](#) and [D’Onofrio et al. \(2019\)](#) investigated the 2D scaling relations in the EAGLE and Illustris simulations, respectively. They found that the observed 2D scaling relations are approximately reproduced by these two simulations. However, these relations show large scatters when projected from the 3D parameter space to 2D. Thus, we directly investigate the scaling relation in the 3D parameter space (the fundamental plane) in this work.

The goal of this paper is multi-fold: (i) to examine whether the IllustrisTNG-100 simulation has produced a FP plane relation among the size, velocity dispersion, and the surface brightness of early-type galaxies; if so, then (ii) to establish how early such a plane relation emerges and how the plane parameters evolve with cosmic time; and most importantly, (iii) to investigate whether this plane is plausible compared to observations, i.e., whether Eq. (6) is met or equivalently, whether a power-law relation between M/L and M has been well produced by the simulation.

The paper is organized as follows. In Section 2, we introduce the simulation (Section 2.1), describe our mock galaxy sample and galaxy morphology classification (Section 2.2), and specify the FP fitting method (Section 2.3). Section 3.1 is devoted to presenting the FP slopes b and c and their redshift evolution. The redshift evolution of the FP scatter, zero point, and the relation between the FP scatter and stellar age are presented in Section 3.2. The relation

between the dynamical mass and the dynamical mass-to-light ratio of the TNG100 early-type galaxies is presented in Section 3.3. Finally, we summarize our findings in Section 4.

2 METHODOLOGY

2.1 The IllustrisTNG Simulations

The Next Generation Illustris Simulations (IllustrisTNG) ([Marinacci et al. 2018](#); [Naiman et al. 2018](#); [Nelson et al. 2018](#); [Pillepich et al. 2018b](#); [Springel et al. 2018](#)) are a suite of state-of-the-art magneto-hydrodynamic cosmological galaxy formation simulations carried out in large cosmological volumes with the moving-mesh code AREPO ([Springel 2010](#)). The IllustrisTNG Simulations are built and improved upon the original Illustris Simulations with the same initial conditions ([Genel et al. 2014](#); [Vogelsberger et al. 2013, 2014a,b](#); [Nelson et al. 2015](#)) but differ in the updated version of the galaxy formation model, including the addition of ideal magneto-hydrodynamics, a new active galactic nucleus (AGN) feedback model that operates at low accretion rates ([Weinberger et al. 2017](#)) and various modifications to the galactic winds, stellar evolution, and chemical enrichment schemes ([Pillepich et al. 2018a](#)). In this work, we use its full-physics version with a cubic box of 110.7 Mpc side length (TNG100); it has been made publicly available³ ([Nelson et al. 2019](#)). The mass resolutions of the TNG100-full physics version for baryonic and dark matter are $m_{\text{baryon}} = 1.4 \times 10^6 M_{\odot}$ and $m_{\text{DM}} = 7.5 \times 10^6 M_{\odot}$, with a gravitational softening length of $\epsilon = 0.74$ kpc. Gas cells are resolved in a fully adaptive manner with a minimum softening length of 0.19 comoving kpc. Galaxies in their host dark matter halos are identified using the SUBFIND algorithm ([Springel et al. 2001](#); [Dolag et al. 2009](#)).

2.2 Early-type galaxy classification and sample selection

We describe our criteria of sample selection and galaxy morphology classification in this section. To start with, we only select central galaxies to compose our sample, excluding all satellite galaxies whose host dark matter subhalos are identified by SUBFIND. Each stellar particle is treated as a coeval stellar population following the [Chabrier \(2003\)](#) initial mass function (IMF). We derive the stellar luminosity using the stellar population synthesis (SPS) model GALAXEV ([Bruzual & Charlot 2003](#)). A semi-analytical dust attenuation treatment is applied to the stellar light based on neutral hydrogen density and metallicity to mock observations (see [Xu et al. 2017](#) for details). Furthermore, we compute the surface brightness profiles within elliptical isophotes determined by the projected luminosity-weighted second moments of the galaxy, and perform a 1D Sérsic profile fitting within 0.05 to 3 times R_{hsm} to obtain the Sérsic index. To ensure that every galaxy in our sample is sufficiently resolved, we only consider galaxies and their associated host dark matter halos with stellar masses $M_{*,30\text{kpc}} \geq 5 \times 10^9 M_{\odot}$. $M_{*,30\text{kpc}}$ is the total stellar mass within a radius of 30 kpc from the galaxy center, for which we adopt the position of the particle with the lowest gravitational potential in its host halo.

Galaxy types are subject to different possible classification criteria. One can define a sample of early-type galaxies based on their

² <http://www.tng-project.org>

³ <http://www.tng-project.org/data/>

more compact morphologies, more dispersion-dominated kinematics, redder colors and/or lower star-formation rates. The sole usage of a single individual criterion does not necessarily yield consistent galaxy-type determination (e.g., Bottrell et al. 2017, Wang et al. 2019a, Donnari et al. 2019). Therefore, we combine the light profile measured in the rest-frame SDSS r -band (Stoughton et al. 2002) with the specific star-formation rate (sSFR) to classify typical central early-type galaxies for this study. Here we set up the two criteria for galaxy-type classification:

(i) Following Xu et al. (2017), we fit both a single de Vaucouleurs profile (de Vaucouleurs 1948) (which is often used to describe the light distribution of an elliptical galaxy) and a single exponential profile (which is often used to describe the light distribution of a disk galaxy) to a galaxy's radial surface brightness distribution. An early-type galaxy should have the de Vaucouleurs model fit its light distribution better than the exponential profile.

(ii) It is a common practice in observations to separate early- and late-type galaxies with a certain specific SFR (sSFR) threshold (McGee et al. 2011; Wetzel et al. 2013; Lin et al. 2014; Jian et al. 2018), which is also used in simulations (Genel et al. 2018). Thus, we follow the practice of Genel et al. (2018) and classify quenched galaxies (early-type galaxies) by quantifying their distance from the ridge of star-forming main-sequence galaxies. The ridge of main-sequence galaxies is defined as the mean specific SFR (sSFR) of galaxies with $M_{*,30\text{kpc}} < 10^{10.5} M_{\odot}$ at each selected redshift. Here we calculate the sSFR in an aperture with three-dimensional half stellar mass radius, R_{hsm} . Galaxies are classified to be quenched if their sSFR is at least 1 dex below the ridge (for more details, see Genel et al. 2018, Appendix A).

If a galaxy satisfies both criteria above in *all* three principal projections (along X, Y and Z axes of the simulation box), it is then classified as an early-type galaxy. In this work, we view our selected galaxies in their X-projection. Fig. 1 shows the $z = 0$ distributions of $\log R_{\text{hsm}}$, SDSS $g - r$ color, luminosity-weighted stellar age within R_{hsm} ($\log \text{Age}$), and Sérsic index ($n_{\text{Sérsic}}$) versus $\log M_{*,30\text{kpc}}$ (see Xu et al. 2017 for detailed descriptions of galaxy property extraction). As can be seen from the figure, the selected early-type galaxies indeed occupy the expected regions in the parameter space: they are typically more massive and bigger, redder and older, and have $n_{\text{Sérsic}} \gtrsim 2$. Note that there are many old, red, and massive galaxies excluded from our samples. That is because they have small Sérsic index ($n_{\text{Sérsic}} < 2$ or disk), even though they are close to ETGs in terms of star formation. Such galaxies have shown to be overproduced in IllustrisTNG (see Rodríguez-Gomez et al. 2019, Fig. 8), so we exclude them from our sample. In addition, there are galaxies with large $n_{\text{Sérsic}} (> 10)$. They typically have power-law outer profiles and are not as cuspy as true $n_{\text{Sérsic}} > 10$ profiles. This may be caused by several factors, such as mis-centering, gravitational softening, and the fact that we exclude the inner regions when we perform Sérsic profile fits (see Xu et al. 2017 for more details).

The above galaxy-type classification and sample selection criteria are applied to galaxies at the following redshifts, $z = [0.0, 0.1, 0.2, 0.3, 0.4, 0.5, 0.7, 1.0, 1.5, 2.0]$, for which full snapshot data exist in the TNG100 simulation. This results in 1064, 944, 852, 745, 665, 606, 513, 365, 200, and 64 early-type galaxies selected at the above-mentioned redshifts, respectively. As the number of early-type galaxies within the required stellar mass range decreases significantly with redshift, the highest redshift in this study is limited to $z = 2.0$ in order to maintain sizeable statistical samples and reliable galaxy morphologies.

We also remind the reader that since the TNG100 simulation contains only a few galaxies which are in clusters, the majority of our sample galaxies are non-cluster early-type galaxies. Therefore we do not aim to address the environmental dependence of the FP relation in this work. We have also visually inspected the morphology of all selected galaxies at different redshifts. We confirm that galaxies that happen to be experiencing merger processes are very rare cases ($\sim 0.5\%$). Therefore our samples do not suffer from significant contamination by on-going merging systems.

2.3 Fundamental plane fitting

We adopt the following mathematical form to describe the FP relation:

$$\log \frac{R_{\text{hsm}}}{\text{kpc}} = a + b \log \frac{\sigma_e}{\text{km s}^{-1}} + c \log \frac{I_e}{L_{\odot} \text{kpc}^{-2}}, \quad (11)$$

where σ_e is the luminosity-weighted root-mean-square velocity of all stellar particles within R_{hsm} calculated along a given line of sight (X-projection); I_e is the rest-frame SDSS r -band mean surface brightness of all stellar particles within R_{hsm} , defined as follows:

$$I_e = \frac{L}{\pi R_{\text{hsm}}^2}, \quad (12)$$

where L is the rest-frame SDSS r -band luminosity of the galaxy projected within R_{hsm} .

We note that for simplicity, R_{hsm} , which is directly measured from simulation data, is used here as an approximation of the commonly used 2D effective radius R_{eff} in observations. We use LTS_PLANEFIT described in Cappellari et al. (2013) to perform plane fitting on galaxies at redshifts shown in Table 1. LTS_PLANEFIT combines the Least Trimmed Squares robust technique of Rousseeuw & van Driessen (2006) into a least-squares fitting algorithm and allows us to take observational error into account and exclude outliers. We also carry out the FP analysis using the aperture with 2D effective radius R_{eff} at several redshifts, which is the effective radius from the best-fit Multi-Gaussian Expansion (MGE)⁴ (Emsellem et al. 1994; Cappellari 2002) formalism of the galaxy's surface brightness distribution, and verify that our main results remain unchanged.

To estimate the errors of the FP coefficients, we employ a bootstrap method. For each sample at a given redshift, we draw 500 bootstrap samples with sizes same as the original sample. Compared to the fitting error of the plane parameters fitted to the original sample, the standard deviations of the FP coefficients from bootstrapping are slightly larger. Thus, we take the standard deviation of the fitted FP coefficients from bootstrapping as the best-fit parameter uncertainties.

3 RESULTS

Table 1 presents the best-fit plane's zero point a , the slope parameters b and c , as well as the scatter Δ and the relative scatter Δ/σ_R at various investigated redshifts, where Δ is the plane scatter and σ_R

⁴ The software is available from <https://www-astro.physics.ox.ac.uk/~mxc/software/>.

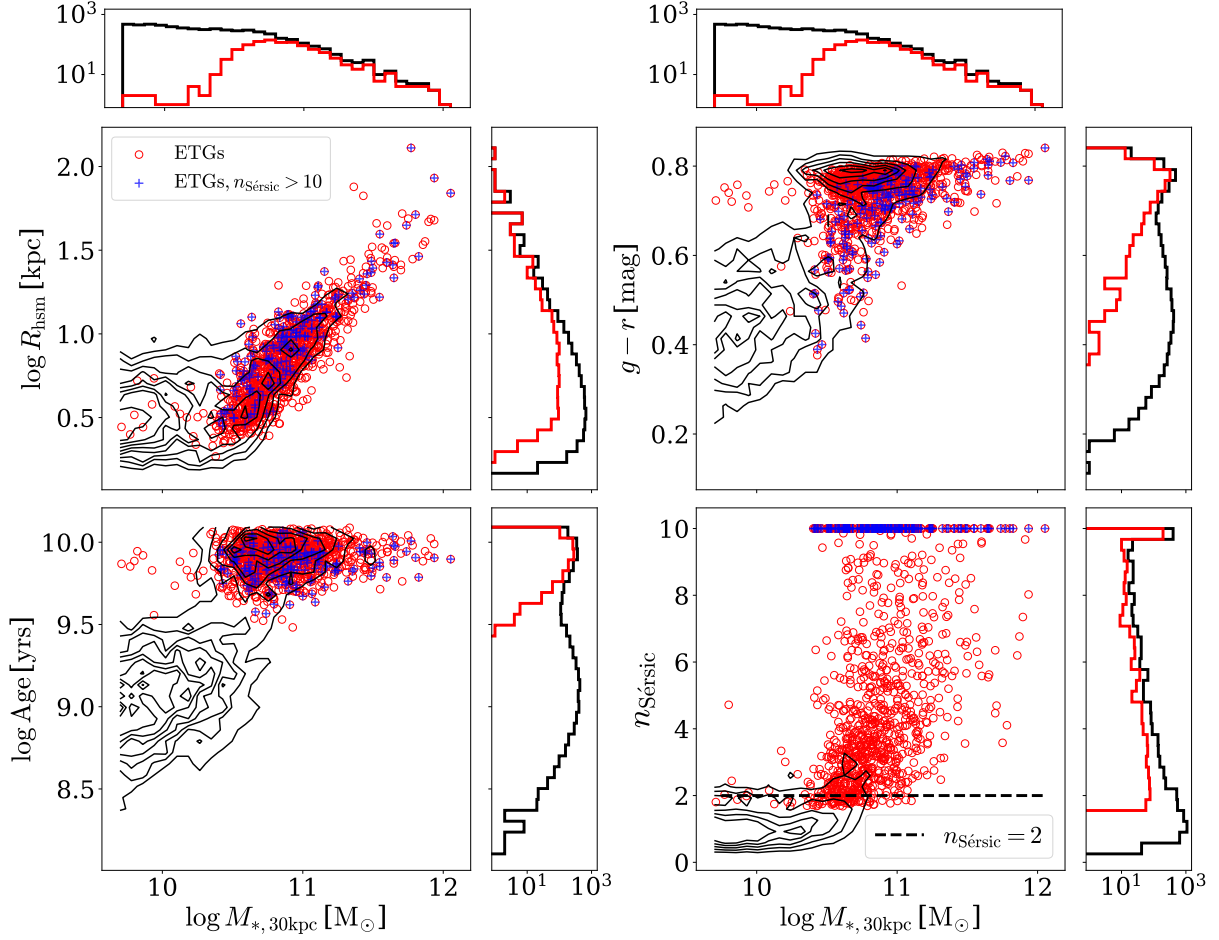


Figure 1. Distributions of the three-dimensional half stellar mass radius $\log R_{\text{hsm}}$, SDSS $g-r$ color, stellar age $\log \text{Age}$, and Sérsic index $n_{\text{Sérsic}}$ versus $\log M_{*,30\text{kpc}}$ for selected early-type galaxies (red circles) and the full sample ($M_{*,30\text{kpc}} \geq 5 \times 10^9 \text{ M}_\odot$) from TNG100 (black contours), respectively. The histograms are the projected distributions of the parameters for both the early-type galaxies (red) and the full sample (black) shown in each panel. The black dashed line in the lower right panel indicates $n_{\text{Sérsic}} = 2$. The upper limit of $n_{\text{Sérsic}}$ is set to be 10 in the lower right panel and galaxies with $n_{\text{Sérsic}} > 10$ are indicated with plus symbols at the centers of the circles in each panel.

is the scatter in $\log R_{\text{hsm}}$. Δ and σ_R are calculated as:

$$\begin{cases} \Delta = \sqrt{\frac{\sum_{i=1}^N \text{Res}_i^2}{N}}, \\ \sigma_R = \sqrt{\frac{\sum_{i=1}^N (\log R_{\text{hsm},i} - \overline{\log R_{\text{hsm}}})^2}{N}}, \end{cases} \quad (13)$$

where N is the total number of selected galaxies at each redshift; Res is the plane residual, which is calculated as $\text{Res} \equiv a + b \log \sigma_e + c \log I_e - \log R_{\text{hsm}}$. Δ/σ_R is the ratio of the scatter after and before the FP fit and can be used to quantify the existence of the plane (van de Sande et al. 2014).

Below, we first present in Section 3.1, the plane rotation, then in Section 3.2, the plane offset and the evolution of the scatter, and in Section 3.3, the relation of the $M_{\text{dyn}}/L - M_{\text{dyn}}$ plane and its implication, where M_{dyn} denotes the dynamical mass.

3.1 The slope parameters b and c and their redshift evolution

Observationally, rotation of the FP over a redshift range out to $z > 1$ has been detected to a certain degree: b with a local value of ~ 1.2 (in B -band) decreases from $b \gtrsim 1$ at intermediate redshifts

below $z \sim 0.8$ (e.g., van Dokkum & Franx 1996; Kelson et al. 2000; Wuyts et al. 2004; van der Marel & van Dokkum 2007; Bolton et al. 2008; Auger et al. 2010; Saglia et al. 2010) to $b \lesssim 0.8$ at $0.8 \lesssim z \lesssim 1.3$ (e.g., di Serego Alighieri et al. 2005; Jørgensen et al. 2006). While c from a local value of ~ -0.8 (e.g., Jørgensen et al. 1996; Bender et al. 1998; Hou & Wang 2015) increases to ~ -0.6 at redshifts $z \gtrsim 0.5$ (di Serego Alighieri et al. 2005; Saglia et al. 2010). It is worth noting that despite this plane rotation, b and c evolve in a fashion such that Eq. (6) is broadly satisfied across the observed redshift ranges within measurement uncertainties⁵.

In comparison, the FP evolution of early-type galaxies from the TNG100 simulation demonstrates relatively mild plane rotation. As can be seen from Table 1, the slope parameters b and c vary only slightly with redshift. To better demonstrate this evolution, we present Fig. 2, where the redshift evolution of the parameters is plotted against current measurements. We note here that only results where the investigated wavelength is close to the SDSS- r band are included in the figure. Compared to observational data, the TNG predicted redshift evolution of b agrees well with obser-

⁵ This still needs further confirmation using more extensive galaxy samples across cosmic time (e.g., see Saglia et al. 2010).

z	N_{gal}	a	b	c	Δ	$\frac{\Delta}{\sigma_R}$	δ
0	1064	3.129 ± 0.128	1.295 ± 0.026	-0.627 ± 0.012	0.078 ± 0.002	0.287 ± 0.010	0.788 ± 0.066
0.1	944	3.194 ± 0.131	1.290 ± 0.027	-0.630 ± 0.011	0.077 ± 0.002	0.282 ± 0.010	0.769 ± 0.068
0.2	852	3.087 ± 0.134	1.324 ± 0.029	-0.624 ± 0.011	0.078 ± 0.002	0.292 ± 0.011	0.829 ± 0.065
0.3	745	3.101 ± 0.157	1.303 ± 0.036	-0.617 ± 0.012	0.076 ± 0.002	0.288 ± 0.011	0.834 ± 0.071
0.4	665	3.023 ± 0.155	1.261 ± 0.033	-0.595 ± 0.012	0.069 ± 0.004	0.274 ± 0.011	0.880 ± 0.070
0.5	606	3.140 ± 0.164	1.241 ± 0.035	-0.602 ± 0.013	0.071 ± 0.004	0.281 ± 0.012	0.835 ± 0.077
0.7	513	3.194 ± 0.167	1.230 ± 0.035	-0.601 ± 0.014	0.077 ± 0.004	0.297 ± 0.013	0.826 ± 0.077
1.0	365	3.009 ± 0.209	1.218 ± 0.041	-0.572 ± 0.017	0.073 ± 0.004	0.280 ± 0.016	0.929 ± 0.093
1.5	200	3.758 ± 0.200	1.119 ± 0.055	-0.616 ± 0.016	0.075 ± 0.004	0.304 ± 0.021	0.656 ± 0.086
2.0	64	3.643 ± 0.363	0.994 ± 0.093	-0.569 ± 0.034	0.079 ± 0.004	0.405 ± 0.048	0.717 ± 0.153

Table 1. The FP fit results for the selected ETG samples. a , b , and c are defined in Eq. (11). Δ is the root-mean-square of the fitting residual $\text{Res} (= a + b \log \sigma_e + c \log I_e - \log R_{\text{hsm}})$. σ_R is the scatter in $\log R_{\text{hsm}}$ (see Section 3 for detailed definitions). δ is defined as $\delta \equiv 4c + b + 2$. The errors of a , b , c , Δ , Δ/σ_R , and δ are calculated with the bootstrap method.

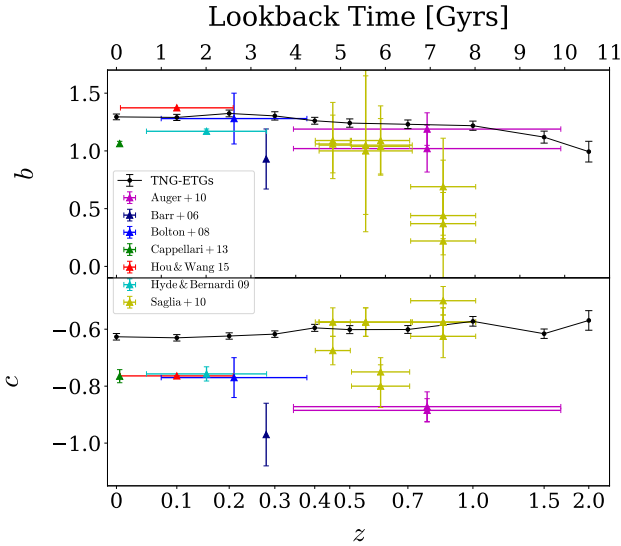


Figure 2. Redshift dependencies of the FP slope parameters b (upper) and c (bottom). The results of the TNG100 ETG samples are indicated by the black circles with error bars calculated with the bootstrap method (see Section 2.3). Triangles with other colors show the observational results at different redshifts, with error bars indicating the uncertainties of the FP slope (b and c) and the redshift range of their samples.

variations at redshifts below $z \lesssim 0.7$, but the magnitude of b becomes marginally higher than observations at higher redshifts; the predicted evolution of c is consistent with observations at $z \gtrsim 0.4$, but appears systematically higher than the observed values at redshifts below $z \sim 0.4$. These inconsistencies may come from the larger sizes (Genel et al. 2018; Rodriguez-Gomez et al. 2019) and lower σ_e (Wang et al. 2020) of IllustrisTNG ETGs compared with observations, as a result of overly-strong AGN feedback (typically the isotropic black hole kinetic winds in the AGN quiescent phase) in IllustrisTNG for puffing up the galaxies (Wang et al. 2019b, 2020).

3.2 The FP zero point a , its scatter and redshift evolution

The zero point of the observed FP changes dramatically with cosmic time. To demonstrate the redshift evolution of a , we present Fig. 3, where the relative zero points ($\Delta a \equiv a - a_{z=0}$) at various

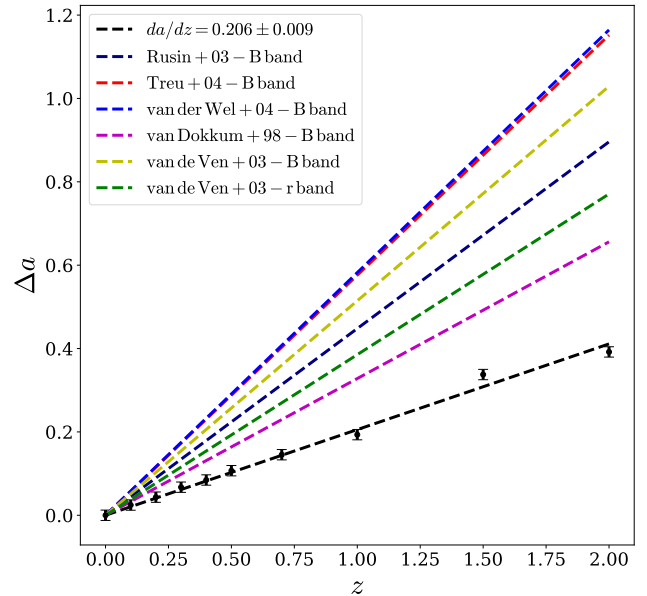


Figure 3. Redshift dependencies of the relative zero point ($\Delta a \equiv a - a_{z=0}$). The error bars are calculated with the bootstrap method. The black dashed line is the best-fit line of the $\Delta a - z$ relation. The dashed lines with colors indicate the best-fit lines of the $\Delta a - z$ relation from observations listed in the legend.

redshifts are plotted. The relative zero points are obtained using fixed plane slopes $b = 1.295$ and $c = -0.627$ (as they evolve mildly with redshift) from the $z = 0$ plane fitting. The zero points of the TNG100 FP have changed by ~ 0.1 , 0.2 , and 0.4 out to $z = 0.5$, 1.0 , and 2.0 , while observationally, the zero points have a steeper relation with redshift than TNG100 FPs (Rusin et al. 2003; Treu & Koopmans 2004; van der Wel et al. 2004; van Dokkum et al. 1998; van de Ven et al. 2003). We note here that the redshifts of observational samples are limited up to $z \sim 1.0$, but we see that the tight linear relation between z and Δa exists as early as $z \sim 2.0$ in TNG100.

Another interesting property of the FP is its tightness. It is related to questions such as how early a FP forms and how the tightness evolves with cosmic time. In order to answer these questions,

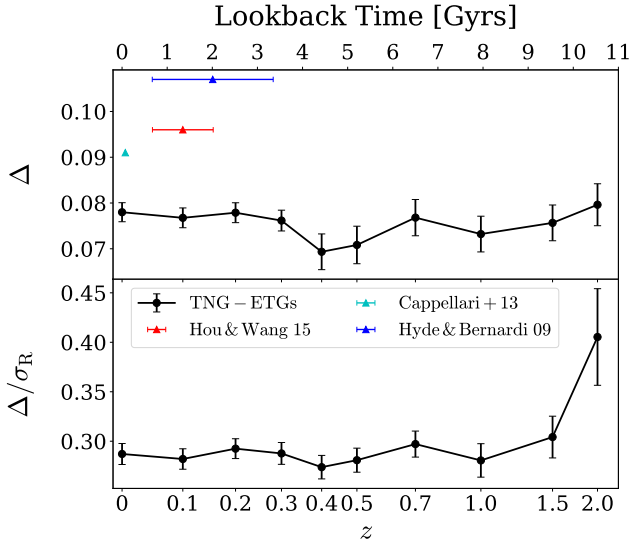


Figure 4. The redshift dependence of Δ (upper) and Δ/σ_R (bottom). The results of the TNG100 ETG samples are indicated by the black circles with error bars calculated with the bootstrap method. In the upper panel, triangles with colors are the results from observational works listed in the legend, with error bars indicating the redshift range of their samples.

we apply Δ to quantify the strength of the FP and Δ/σ_R to quantify the existence of the FP (see Eq. 13 for detailed definitions).

From Table 1, we have already seen that the FP exists as early as $z = 2.0$ in the sense that its scatter Δ (and Δ/σ_R) is already small by then. We further present the redshift evolution for Δ and Δ/σ_R in Fig. 4. As can be seen, the relative scatter Δ/σ_R decreases from ~ 0.4 at $z = 2.0$ to as low as ~ 0.3 at $z = 1.5$, and stays nearly constant since then. The FP scatter, however, never undergoes an obvious variation across the various redshift ranges. Observationally, the observed scatter of the FP varies a lot from 0.091 (Cappellari et al. 2013) to 0.107 (Hyde & Bernardi 2009), showing an increasing trend towards high redshift. However, the FP scatter of simulated galaxies are typically lower than observed ones.

The FP scatter has been identified to be linked to aging stellar populations in early-type galaxies (van Dokkum & Franx 1996; Forbes et al. 1998; Terlevich & Forbes 2002). In order to see such a connection, we present Fig. 5, where the left panel shows the $z = 0$ FP color-coded by the ETGs’ stellar age $\log \text{Age}$, which is calculated as the luminosity-weighted age within an aperture of R_{hsm} , and the right panel shows the correlation between the plane residual (Res) and $\log \text{Age}$. As can be seen, the FP residual (Res) tightly correlates with age: it increases by ~ 0.4 dex as $\log \text{Age}$ changes from ~ 9.5 to ~ 10 . This trend is also seen in observations (Forbes et al. 1998; Terlevich & Forbes 2002; Graves et al. 2009; Springob et al. 2012; Magoulas et al. 2012). We have also investigated the correlations between the FP residual (Res) and other properties of galaxies in TNG, i.e., metallicity and mass-to-light ratio and find that the correlations still exist. However, stellar age shows the strongest correlation with the FP residual, which is consistent with the observational results (Magoulas et al. 2012). This indicates that our ETG sample selected from TNG100 supports the scenario where the galaxy stellar age is the fourth parameter of the FP relation (Forbes et al. 1998).

3.3 A plane versus THE plane: $\log M_{\text{dyn}}/L - \log M_{\text{dyn}}$ relation

The seemingly mild inconsistencies between the simulated and observationally-constrained plane slopes b and c at various redshifts (as shown in Fig. 2) actually point to an interesting theoretical question: how plausible is the plane relation seen in TNG100 compared to observations, given that the observed FPs till now satisfy Eq. (6) within their measurement uncertainties. To quantify this, we can define $\delta \equiv 4c + b + 2$ at any given redshift and quantify how well the measurement of δ is clustered around zero, given the model uncertainties. For observational results, the measurement uncertainties of δ are calculated as $\sqrt{\sigma_b^2 + (4\sigma_c)^2}$, with σ_b and σ_c being the measurement uncertainties of b and c . For TNG FPs, the measurement uncertainties of δ are calculated with the bootstrap method. We present Fig. 6 to show the values of δ at every redshift investigated in our work and compare them with observations (Barr et al. 2006; Bolton et al. 2008; Hyde & Bernardi 2009; Auger et al. 2010; Saglia et al. 2010; Cappellari et al. 2013; Hou & Wang 2015). As can be seen, δ of the FPs in TNG are typically larger than 0, which is inconsistent with the prediction of Eq. (6). Note that the errors of b and c for TNG FPs are somewhat underestimated because we did not take into account the measurement uncertainties of $\log R_{\text{hsm}}$, $\log L_e$, and $\log \sigma_e$. However, even if the errors of b and c are increased by a factor of ~ 3 , $\delta = 0$ is still not satisfied. In contrast, the observed FPs’ δ are clustered around 0 at various redshifts. The average observational value for δ is 0.120, with the 1σ range being 0.109, indicating that $\delta = 0$ is satisfied by the observed FPs at 1σ level. We note here that the 1σ range of observational δ is estimated as the intrinsic scatter, calculated as the square root of the difference between the variance of the observational δ and the average of their measurement uncertainties squared.

As already discussed in Section 1, $\delta = 0$ is equivalent to the fact that a certain dynamical mass-to-light ratio $\log M_{\text{dyn}}/L$ (where $M_{\text{dyn}} \equiv 5\sigma_e^2 R_{\text{hsm}}/G$, Bender et al. 1992) would follow a linear function of $\log M_{\text{dyn}}$. To see how well such a relation is met by our simulated ETGs, we present Fig. 7, where $\log M_{\text{dyn}}/L$ versus $\log M_{\text{dyn}}$ is plotted⁶ for galaxies at $z = 0, 1$, and 2 in our samples. A linear fit of $\log M_{\text{dyn}}/L - \log M_{\text{dyn}}$ is applied, with the coefficient of determination \mathcal{R}^2 indicating the goodness of linear fit. As can be seen, the \mathcal{R}^2 of each fit is low ($\lesssim 0.7$), indicating that $\log M_{\text{dyn}}/L$ does not have an acceptable linear relation with $\log M_{\text{dyn}}$. In addition, observed galaxies have shown strong evolution of the slope of the $\log M_{\text{dyn}}/L - \log M_{\text{dyn}}$ relation (e.g., Jørgensen et al. 2006; Saglia et al. 2010; Holden et al. 2005), which is, however, not seen for TNG100 early-type galaxies. Thus, the deviation from $\delta = 0$ for TNG100 ETGs arises from the combination of a loose $\log M_{\text{dyn}}/L - \log M_{\text{dyn}}$ linear relation and a lack of evolution of the slope of this linear relation, which indicates that the tight FP in TNG100 is ultimately not consistent with the observations.

4 CONCLUSION AND DISCUSSION

In this work, we have used early-type galaxies (ETGs) in the IllustrisTNG-100 simulation (TNG100) from $z = 0$ to $z = 2$ to study the evolution of the fundamental plane (the slopes, scatter, and zero point). We found that the FP slopes b and c vary mildly across the redshift range $z \in [0, 2]$. The slope parameter

⁶ Note that this is essentially the same as the $\sqrt{3}\kappa_3 - \sqrt{2}\kappa_1$ projection of the FP relation (see Bender et al. 1992).

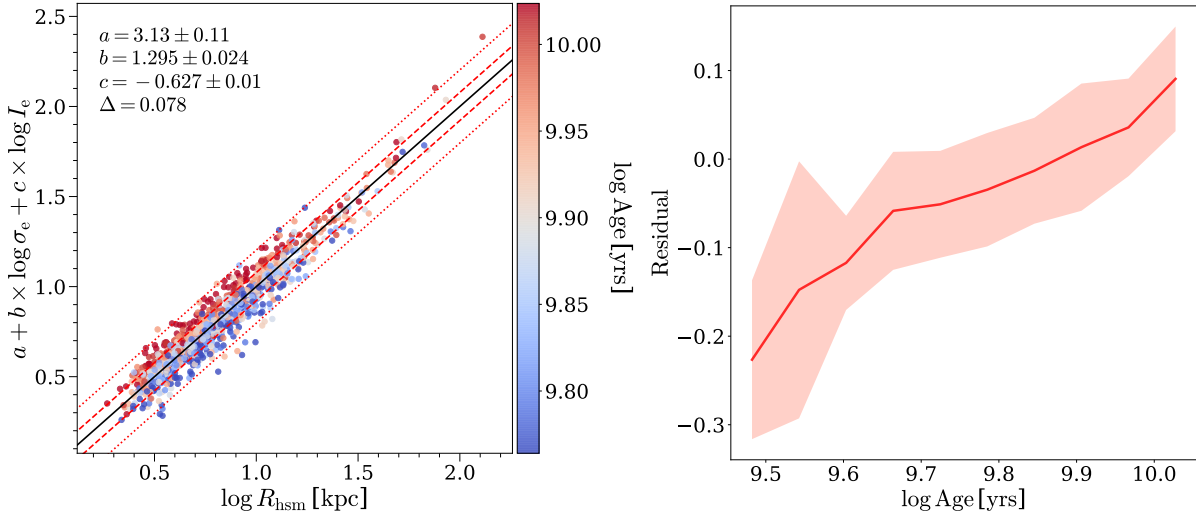


Figure 5. Left panel: Edge-on view of the best-fit fundamental plane for early-type galaxies at $z = 0$ in TNG100, color-coded by their stellar age, $\log \text{Age}$. The black solid line is the best-fit plane and the red dashed lines show the 68% (1σ) and 99% confidence intervals. Right panel: Relation between the FP residual, Res , and the stellar age, $\log \text{Age}$. The FP residual is calculated as $\text{Res} = a + b \times \log \sigma_e + c \times \log I_e - \log R_{\text{hsm}}$. The red shaded region represents the 1σ range of residual.

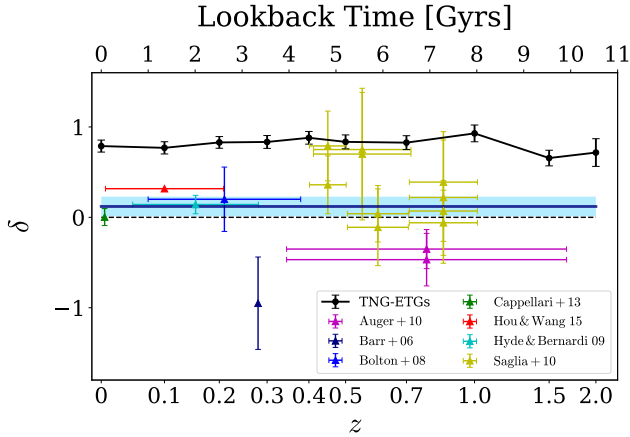


Figure 6. Redshift dependence of $\delta \equiv 4c + b + 2$. The results of TNG100 samples are indicated by the black circles and observational results are indicated by triangles with colors. For observational results, the errors of δ are calculated as $\sqrt{\sigma_b^2 + (4\sigma_c)^2}$, where σ_b and σ_c are the plane fit errors. For TNG-ETGs, the errors of δ are calculated with the bootstrap method. The black dashed line represents $\delta = 0$. The blue solid line represents the average value of δ for the observations, with the shaded region indicating the 1σ range of δ .

values at various redshifts are roughly consistent with observations within measurement uncertainties. In particular, for b , the result of TNG100 agrees with observations at $z \lesssim 0.7$, but is slightly higher at $z > 0.7$. For c , the result of TNG100 is consistent with the observations at $z > 0.4$, but is higher than the observational constraints at redshifts below 0.4.

We have also examined the relation between the relative zero point ($\Delta a \equiv a - a_{z=0}$) and the redshift for TNG100 FPs using fixed slope parameters $b = 1.295$ and $c = -0.627$ of the FP at $z = 0$. We find that the tight linear relation between Δa and redshift found in observations is also seen in TNG100, but is somehow flatter than

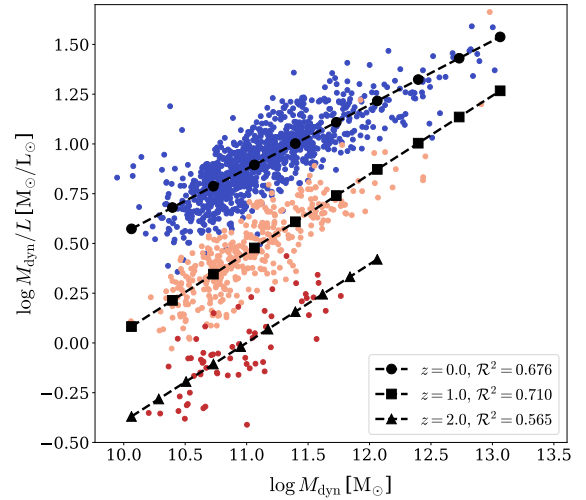


Figure 7. Relation between the dynamical mass-to-light ratio ($\log M_{\text{dyn}}/L$, where $M_{\text{dyn}} \equiv 5\sigma_e^2 R_{\text{hsm}}/G$) and the dynamical mass ($\log M_{\text{dyn}}$) of galaxies at $z = 0, 1$, and 2 . The dashed lines with different markers give the best linear-fit lines of the $\log M_{\text{dyn}}/L$ - $\log M_{\text{dyn}}$ relation at each redshift. \mathcal{R}^2 is the coefficient of determination.

the observational results ($da/dz \sim 0.33 - 0.58$ in observations, but 0.206 in TNG100). In observations, the results are limited to $z \sim 1.0$ due to the lack of high redshift samples, while in TNG100, galaxies at higher redshift ($z \sim 2.0$) are also found to obey this linear relation.

The scatter Δ of the FP in TNG100 stays as low as $\lesssim 0.8$ dex and is nearly unchanged since $z = 2.0$, while Δ/σ_R (see Section 3.2 for its definition) decreases from ~ 0.4 at $z = 2.0$ to ~ 0.3 at $z = 1.5$, and remains constant since then. This implies that the tight fundamental plane relation exists as early as $z = 2.0$. In com-

parison, the FP scatter of TNG100 ETGs is typically lower than those in observations. Observationally, the FP scatter varies significantly from 0.091 to 0.107 across redshifts up to $z \sim 0.155$, with an increasing trend towards higher redshifts.

To see the origin of the FP scatter, we have investigated where galaxies with different stellar ages are located on the edge-on view of the FP at $z = 0$. We find that older galaxies sit near the ‘top’ of the plane, and younger galaxies vice versa. The FP residual, which is calculated as $\text{Res} \equiv a + b \log \sigma_e + c \log I_e - \log R_{\text{hsm}}$, strongly correlates with stellar age, indicating the fact that stellar age can be used as a crucial fourth parameter of the FP as pointed out by Forbes et al. (1998).

An interesting piece of observational evidence is that the observed FPs more or less satisfy Eq. (6). To quantify this, we define $\delta \equiv 4c + b + 2$ and find that $\delta = 0$ is satisfied by observed FPs at 1σ level. We find that for TNG100 FPs, however, this condition is not satisfied. As can be seen in Fig. 6, the δ for TNG100 FPs is significantly inconsistent with $\delta = 0$. This suggests that the plane relation in TNG100, despite being tight, is not an observationally plausible plane.

The inconsistency with $\delta = 0$ indicates that the tight linear relation between the dynamical mass-to-light ratio $\log M_{\text{dyn}}/L$ and the dynamical mass $\log M_{\text{dyn}}$ (or equivalently the $\kappa_3 - \kappa_1$ relation in Bender et al. 1992) found in observations is not reproduced by the TNG100 simulation. This is confirmed in Fig. 7 where the $\log M_{\text{dyn}}/L - \log M_{\text{dyn}}$ relation has low coefficients of determination (R^2). In addition, no redshift evolution of the slope for the $\log M_{\text{dyn}}/L - \log M_{\text{dyn}}$ relation is seen for the simulated galaxies, whereas the observed samples suggest a strong redshift evolution.

Due to the diversification of the causes in shaping a galaxy, the $\log M_{\text{dyn}}/L - \log M_{\text{dyn}}$ relation (or the $\delta = 0$ condition) requires early-type galaxies to have the ‘correct’ mixing between dark matter and baryons. In addition, halo assembly and galaxy formation are both shaped by various baryonic physical processes on smaller scales, as well as complicated merger and accretion environments on larger scales. Thus, the ‘correct’ star-formation efficiencies that occur at a wide range of galaxy and halo mass scales are also required to form such a relation. In observations, $\delta = 0$ is broadly satisfied, indicating that the observed early-type galaxies are well ‘tuned’. The simulated ETGs in TNG100, however, do not possess such properties. As an outlook, we suggest that in future simulations, tight power-law relations between M_{dyn}/L and M_{dyn} should be sought as some extra constraint to validate the simulations in terms of internal dynamical structure of galaxies in order to better reproduce galaxy populations which are observationally fully consistent.

ACKNOWLEDGEMENTS

We thank Dylan Nelson for helpful suggestions to this work. This work is partly supported by a joint grant between the DFG and NSFC (Grant No. 11761131004), the National Key Basic Research and Development Program of China (No. 2018YFA0404501), and grant 11761131004 of NSFC to SM.

REFERENCES

Auger M. W., Treu T., Bolton A. S., Gavazzi R., Koopmans L. V. E., Marshall P. J., Moustakas L. A., Burles S., 2010, *ApJ*, **724**, 511
Barr J., Jørgensen I., Chiboucas K., Davies R., Bergmann M., 2006, *ApJ*, **649**, L1

Bender R., Burstein D., Faber S. M., 1992, *ApJ*, **399**, 462
Bender R., Saglia R. P., Ziegler B., Belloni P., Greggio L., Hopp U., Bruzual G., 1998, *ApJ*, **493**, 529
Bernardi M., et al., 2003, *AJ*, **125**, 1866
Bernardi M., Nichol R. C., Sheth R. K., Miller C. J., Brinkmann J., 2006, *AJ*, **131**, 1288
Bertin G., Ciotti L., Del Principe M., 2002, *A&A*, **386**, 149
Biermann P., Shapiro S. L., 1979, *ApJ*, **230**, L33
Bolton A. S., Treu T., Koopmans L. V. E., Gavazzi R., Moustakas L. A., Burles S., Schlegel D. J., Wayth R., 2008, *ApJ*, **684**, 248
Bottrell C., Torrey P., Simard L., Ellison S. L., 2017, *MNRAS*, **467**, 1033
Bruzual G., Charlot S., 2003, *MNRAS*, **344**, 1000
Busarello G., Longo G., Feoli A., 1992, *A&A*, **262**, 52
Cappellari M., 2002, *MNRAS*, **333**, 400
Cappellari M., 2016, *ARA&A*, **54**, 597
Cappellari M., et al., 2006, *MNRAS*, **366**, 1126
Cappellari M., et al., 2013, *MNRAS*, **432**, 1709
Chabrier G., 2003, *PASP*, **115**, 763
Chevance M., Weijmans A.-M., Damjanov I., Abraham R. G., Simard L., van den Bergh S., Caris E., Glazebrook K., 2012, *ApJ*, **754**, L24
Ciotti L., Lanzoni B., Renzini A., 1996, *MNRAS*, **282**, 1
Crain R. A., et al., 2015, *MNRAS*, **450**, 1937
D’Onofrio M., Chiosi C., Sciarra M., Marziani P., 2019, arXiv e-prints, p. arXiv:1907.09367
Davies R. L., Efstathiou G., Fall S. M., Illingworth G., Schechter P. L., 1983, *ApJ*, **266**, 41
Djorgovski S., Davis M., 1987, *ApJ*, **313**, 59
Dolag K., Borgani S., Murante G., Springel V., 2009, *MNRAS*, **399**, 497
Donnari M., et al., 2019, *MNRAS*, **485**, 4817
Dressler A., Lynden-Bell D., Burstein D., Davies R. L., Faber S. M., Terlevich R., Wegner G., 1987, *ApJ*, **313**, 42
Dubois Y., et al., 2014, *MNRAS*, **444**, 1453
Emsellem E., Monnet G., Bacon R., 1994, *A&A*, **285**, 723
Faber S. M., Jackson R. E., 1976, *ApJ*, **204**, 668
Faber S. M., Dressler A., Davies R. L., Burstein D., Lynden Bell D., Terlevich R., Wegner G., 1987, in Faber S. M., ed., *Nearly Normal Galaxies. From the Planck Time to the Present*, pp 175–183
Fan L., Lapi A., De Zotti G., Danese L., 2008, *ApJ*, **689**, L101
Ferrarese L., Merritt D., 2000, *ApJ*, **539**, L9
Forbes D. A., Ponman T. J., Brown R. J. N., 1998, *ApJ*, **508**, L43
Genel S., et al., 2014, *MNRAS*, **445**, 175
Genel S., et al., 2018, *MNRAS*, **474**, 3976
Graham A., Colless M., 1997, *MNRAS*, **287**, 221
Graves G. J., Faber S. M., Schiavon R. P., 2009, *ApJ*, **698**, 1590
Gregg M. D., 1992, *ApJ*, **384**, 43
Holden B. P., et al., 2005, *ApJ*, **620**, L83
Hopkins P. F., et al., 2009, *MNRAS*, **397**, 802
Hou L., Wang Y., 2015, *Research in Astronomy and Astrophysics*, **15**, 651
Humphrey P. J., Buote D. A., 2010, *MNRAS*, **403**, 2143
Husemann B., Bennert V. N., Scharwächter J., Woo J.-H., Choudhury O. S., 2016, *MNRAS*, **455**, 1905
Hyde J. B., Bernardi M., 2009, *MNRAS*, **396**, 1171
Jian H.-Y., et al., 2018, *PASJ*, **70**, S23
Jørgensen I., Franx M., Kjaergaard P., 1996, *MNRAS*, **280**, 167
Jørgensen I., Chiboucas K., Flint K., Bergmann M., Barr J., Davies R., 2006, *ApJ*, **639**, L9
Kelson D. D., Illingworth G. D., van Dokkum P. G., Franx M., 2000, *ApJ*, **531**, 184
Khochfar S., Silk J., 2006, *ApJ*, **648**, L21
Kobayashi C., 2005, *MNRAS*, **361**, 1216
Kormendy J., Richstone D., 1995, *ARA&A*, **33**, 581
La Barbera F., Busarello G., Merluzzi P., de la Rosa I. G., Coppola G., Haines C. P., 2008, *ApJ*, **689**, 913
Lanzoni B., Cappi A., Ciotti L., 2003, *Memorie della Societa Astronomica Italiana Supplementi*, **1**, 145
Lin L., et al., 2014, *The Astrophysical Journal*, **782**, 33
Magorrian J., et al., 1998, *AJ*, **115**, 2285
Magoulas C., et al., 2012, *MNRAS*, **427**, 245

- Marinacci F., et al., 2018, *MNRAS*, **480**, 5113
- McGee S. L., Balogh M. L., Wilman D. J., Bower R. G., Mulchaey J. S., Parker L. C., Oemler A., 2011, *MNRAS*, **413**, 996
- Naiman J. P., et al., 2018, *MNRAS*, **477**, 1206
- Nelson D., et al., 2015, *Astronomy and Computing*, **13**, 12
- Nelson D., et al., 2018, *MNRAS*, **475**, 624
- Nelson D., et al., 2019, *Computational Astrophysics and Cosmology*, **6**, 2
- Nipoti C., Londrillo P., Ciotti L., 2002, *MNRAS*, **332**, 901
- Pahre M. A., Djorgovski S. G., de Carvalho R. R., 1995, *ApJ*, **453**, L17
- Pahre M. A., Djorgovski S. G., de Carvalho R. R., 1998a, *AJ*, **116**, 1591
- Pahre M. A., de Carvalho R. R., Djorgovski S. G., 1998b, *AJ*, **116**, 1606
- Pillepich A., et al., 2018a, *MNRAS*, **473**, 4077
- Pillepich A., et al., 2018b, *MNRAS*, **475**, 648
- Prugniel P., Simien F., 1996, *A&A*, **309**, 749
- Renzini A., Ciotti L., 1993, *ApJ*, **416**, L49
- Rodriguez-Gomez V., et al., 2019, *MNRAS*, **483**, 4140
- Rosito M. S., Tissera P. B., Pedrosa S. E., Lagos C. D. P., 2019, *A&A*, **629**, L3
- Rousseeuw P. J., van Driessen K., 2006, *Data Mining and Knowledge Discovery*, **12**, 29
- Rusin D., et al., 2003, *ApJ*, **587**, 143
- Saglia R. P., et al., 2010, *A&A*, **524**, A6
- Schaye J., et al., 2015, *MNRAS*, **446**, 521
- Schombert J. M., 1986, *ApJS*, **60**, 603
- Springel V., 2010, *MNRAS*, **401**, 791
- Springel V., White S. D. M., Tormen G., Kauffmann G., 2001, *MNRAS*, **328**, 726
- Springel V., et al., 2018, *MNRAS*, **475**, 676
- Springob C. M., et al., 2012, *MNRAS*, **420**, 2773
- Stoughton C., et al., 2002, *AJ*, **123**, 485
- Subramanian S., Ramya S., Das M., George K., Sivarani T., Prabhu T. P., 2016, *MNRAS*, **455**, 3148
- Taranu D., Dubinski J., Yee H. K. C., 2015, *ApJ*, **803**, 78
- Terlevich A. I., Forbes D. A., 2002, *MNRAS*, **330**, 547
- Toomre A., Toomre J., 1972, *ApJ*, **178**, 623
- Treu T., Koopmans L. V. E., 2004, *ApJ*, **611**, 739
- Treu T., et al., 2005, *ApJ*, **633**, 174
- Trujillo I., Burkert A., Bell E. F., 2004, *ApJ*, **600**, L39
- Valentinuzzi T., et al., 2010, *ApJ*, **721**, L19
- Vogelsberger M., Genel S., Sijacki D., Torrey P., Springel V., Hernquist L., 2013, *MNRAS*, **436**, 3031
- Vogelsberger M., et al., 2014a, *MNRAS*, **444**, 1518
- Vogelsberger M., et al., 2014b, *Nature*, **509**, 177
- Wang L., Xu D., Gao L., Guo Q., Qu Y., Pan J., 2019a, *MNRAS*, **485**, 2083
- Wang Y., et al., 2019b, *MNRAS*, **490**, 5722
- Wang Y., et al., 2020, *MNRAS*, **491**, 5188
- Weinberger R., et al., 2017, *MNRAS*, **465**, 3291
- Wetzel A. R., Tinker J. L., Conroy C., van den Bosch F. C., 2013, *MNRAS*, **432**, 336
- Wuyts S., van Dokkum P. G., Kelson D. D., Franx M., Illingworth G. D., 2004, *ApJ*, **605**, 677
- Xu D., Springel V., Sluse D., Schneider P., Sonnenfeld A., Nelson D., Vogelsberger M., Hernquist L., 2017, *MNRAS*, **469**, 1824
- de Vaucouleurs G., 1948, *Annales d'Astrophysique*, **11**, 247
- di Serego Alighieri S., et al., 2005, *A&A*, **442**, 125
- van Albada T. S., Bertin G., Stiavelli M., 1995, *MNRAS*, **276**, 1255
- van Dokkum P. G., Franx M., 1996, *MNRAS*, **281**, 985
- van Dokkum P. G., Franx M., Kelson D. D., Illingworth G. D., 1998, *ApJ*, **504**, L17
- van Dokkum P. G., Franx M., Kelson D. D., Illingworth G. D., 2001, *ApJ*, **553**, L39
- van Dokkum P. G., et al., 2008, *ApJ*, **677**, L5
- van de Sande J., Kriek M., Franx M., Bezanson R., van Dokkum P. G., 2014, *ApJ*, **793**, L31
- van de Ven G., van Dokkum P. G., Franx M., 2003, *MNRAS*, **344**, 924
- van der Marel R. P., van Dokkum P. G., 2007, *ApJ*, **668**, 756
- van der Wel A., Franx M., van Dokkum P. G., Rix H.-W., 2004, *ApJ*, **601**, L5
- van der Wel A., Franx M., van Dokkum P. G., Rix H.-W., Illingworth G. D., Rosati P., 2005, *ApJ*, **631**, 145
- van der Wel A., et al., 2011, *ApJ*, **730**, 38